

**Approved  
FLNP Director**

**E.V. Lychagin**

«    » \_\_\_\_\_ 2023 г.

**Report on the theme “Modern Trends and Developments in Raman Microspectroscopy and Photoluminescence for Condensed Matter Studies” and project Biophotonics”  
for the years of 2021-2023.**

**Theme #: 04-4-1133-2018/2023**

**Theme leaders: G.M. Arzumanyan, N. Kučerka**

**Project leaders: G.M. Arzumanyan, N. Kučerka**

**In 2021 - 2023, the research activities of the Sector of Raman spectroscopy of the FLNP were carried out in accordance with the main objectives of the Theme # 1133: "Modern Trends and Developments in Raman Microspectroscopy and Photoluminescence for Condensed Matter Studies" and the project "Biophotonics" in the frame of the Theme.**

Along with neutron and synchrotron studies, optical spectroscopy, including Raman spectroscopy, has its own specific niche in the study of the properties, structure, and diagnostics of condensed matter. Raman spectroscopy is a powerful analytical tool with a wide range of capabilities. This method is based on inelastic scattering of incident radiation on the sample. The frequency shift of the incident radiation corresponds to the vibrational energy of certain bonds in the molecule. Vibrational spectra are extremely specific and sensitive characteristics of molecules. The advantages of Raman spectroscopy are primarily its high sensitivity, non-invasiveness, and the lack of the need for external markers (fluorophores) to visualize the sample under study. Both Raman and FT-IR spectroscopy provide a spectral signature of molecular vibrations ("molecular imprint") and are used to determine the chemical structure of the sample. In doing so, Raman spectroscopy can provide additional information on low-frequency modes and vibrations which indicate features of the crystal lattice and molecular structure. To this end, one of the methodological objectives of the theme was to master the technique of low-frequency Raman spectroscopy.

The “Biophotonics” project is aimed at fundamental and applied research in the field of spontaneous and nonlinear Raman microspectroscopy. One block of tasks was related to the study of the mechanisms and nature of the anomalous ratio of the intensities of the antiStokes (aSt) and Stokes (St) lines in the spectra of surface-enhanced Raman spectroscopy (SERS). The second major block of research concerned a number of tasks in the field of Life Sciences using Raman spectroscopy and fluorescence microscopy. In particular, this concerned the fundamental issues of revealing the mechanisms and signaling pathways of photoinduced netosis (programmed cell death), the search for spectral markers of this phenomenon, as well as some features of the lipid–protein interaction in various membrane mimetics.

## Expected main results upon completion of the theme stages or projects:

- Revealing the features of the ratio of the intensity of the Raman peaks aSt/St in SERS spectra depending on the power of the pump radiation and the laser pumping mode.
- Identification of conformational transitions in the lipid bilayer upon addition of cholesterol and melatonin of various concentrations. Comparison of results with neutron scattering.
- Analysis and interpretation of Raman spectra of liposomes/lipodisks with embedded membrane proteins and "empty" liposomes/lipodisks.
- Obtaining new information about the structure of membrane mimetics with embedded proteins.
- Search for spectral/Raman markers of NETosis.
- Determination of the mechanisms of NETs formation under the action of UV and visible radiation.
- Development of an ultra-low frequency Raman spectroscopy technique  $\sim 10 \text{ cm}^{-1}$ .

### Detailed presentation of scientific results for the years of 2021-2023

## 1. Investigation of an anomaly in the line strength ratios of the aSt / St in the SERS spectra depending on the power density and the pumping mode.

### 1.1 Motivation.

Surface-enhanced Raman scattering spectra, along with large signal strength, manifest a number of distinct features as compared with the spectra of spontaneous Raman scattering recorded under "normal" (non-SERS) conditions. In particular, this refers to the anti-Stokes-to-Stokes molecular spectral line strength ratios (aS/S ratios). This ratios in spontaneous Raman scattering, if far away from electronic resonances, and in case of thermodynamic equilibrium, is defined by the Boltzmann relation corrected by the scattering frequency factor, that is

$$R_{aS}/R_S = (\nu_L + \nu_V)^3 / (\nu_L - \nu_V)^3 \times \exp(-h c \nu_V / k T), \quad (1)$$

where  $R_{aS}$  and  $R_S$  are the anti-Stokes and Stokes scattering rates in [photon/s];  $\nu_L$  and  $\nu_V$  are the frequencies of the incident excitation radiation and of a Raman-active vibrational mode, in  $\text{cm}^{-1}$ ; and  $h$ ,  $c$ , and  $k$  are the Planck constant, the speed of light, and the Boltzmann constant, respectively. This ratio is primarily determined by the relative populations of the upper and lower levels of the transitions involved.

The analysis of the experimental results obtained while investigating SERS spectra showed that in many cases, relation 1 is not valid, even if a wavelength dependence of a local electromagnetic field enhancement factor (LFEF) is taken into account. The attention to this problem increased after the paper by Kneipp et al, published in 1996, where the authors for the first time reported the evidence of optical (Raman) pumping of vibrational states under conditions of SERS. The interpretation of the experimental results involving optical pumping has become the subject of considerable debate in the literature, with many authors denying the existence of the effect and attributing the experimental observations either to laser heating, or to LSPR contributions, or to their combinations.

All this motivated us to conduct research on this topic ourselves. Thus, the aim of the present study is to specify and quantify the role of the mechanisms responsible for the observed discrepancy of the aS/S ratios from those defined by the Boltzmann relation for thermal equilibrium populations of the upper and lower vibrational levels, corresponding to the Raman-active transitions being excited.

### 1.2 Experimental

In this work, the features of an excitation-intensity dependence of the aS/S ratios in SERS spectra in a definite point of a randomly nanostructured SERS-active surface are investigated under CW

785-nm laser illumination at low intensities, which ensure reproducibility of SERS spectral profiles. The near-infrared (NIR) laser is selected for the measurements because it is favorable for investigations of biological samples, which being the main objects for numerous practical SERS studies are transparent in the NIR wavelength range. As Raman reporter molecules, moieties of biochemically relevant organic 5,50-dithiobis (2-nitrobenzoic acid) (DTNB) molecules — thiolates of 2-nitrobenzoic acid (TNB) — covalently bound to nanoscale Ag particles on a porous Si (por-Si) substrate are employed. The particles with various dimensions, shapes, and distances from each other stochastically cover the substrate and form a diversity of 3D nanostructures on its surface with a wide variety of coupled LSPRs.

The power density dependences of the line strength ratio for three respective pairs of vibrational lines of a thiolate of 2-nitrobenzoic acid (TNB) in SERS spectra were derived. Using this data, we specify and quantify the contributions responsible for the discrepancy between this ratio and that defined by the thermal equilibrium populations of the upper and lower vibrational levels corresponding to the Raman-active transitions. These contributions are the following:

- (i) the spectral profile of an LSPR contour,
- (ii) local heating of the reporter molecule/AgP conjugates by the 785-nm radiation, and
- (iii) optical (Raman) pumping of the upper vibrational levels of the transitions involved.

### **1.2.1 Raman setup, samples and results**

A 3D scanning laser confocal Raman microscope (Confotec NR500, SOL Instruments Ltd., Belarus) was employed for SERS-spectra recording. Radiation of a CW narrowband single mode diode laser at  $\lambda_L = 785$  nm (0785L-21A-NI-NT-NF, Integrated Optics, Lithuania) with a power up to 130 mW was used for excitation. The small-divergence laser beam was focused on the sample surface using an inverted microscope (TE2000S, NIKON) with an Olympus MPLFLN 40 x 0.75 NA objective. The beam spot diameter on the surface was  $\approx 1$   $\mu\text{m}$ . The excitation intensity was adjusted by using calibrated neutral density filters.

The backscattered light collected by the objective was directed to the entrance slit of a 520-mm focal length grating monochromator-spectrograph with a 150 grooves per millimeter grating providing the dispersion 12.6 nm/mm. A multilayer dielectric single-notch filter (StopLine NF03-785E-25, Semrock), with the coefficient of suppression of  $>10^6$  within the bandwidth of  $\approx 40$  nm, blocked the reflected and Rayleigh-scattered excitation laser light and enabled recording the spectra simultaneously in the anti-Stokes and Stokes ranges. The transmitting optics made it possible to detect Raman-scattered radiation at the wavenumbers from  $-3260$   $\text{cm}^{-1}$  (at 625 nm) to  $2075$   $\text{cm}^{-1}$  (at 938 nm) in the anti-Stokes and Stokes ranges, respectively.

To assess the homogeneity of the analyte SERS-spectra line strength distribution over the sample surface and to find the sites at the surface with the largest local field enhancement for further detailed investigations of the of the aS/S ratio excitation-intensity dependence, the spectral mapping of this surface was performed.

The SERS-active substrate employed in the experiments was a randomly nanostructured surface of silver particles deposited on a porous silicon surface. Porosity and mean pore diameter of the porous material were 72% and 60 nm, correspondingly. Formation of AgPs on the por-Si samples was carried out by immersion deposition in 3 mM  $\text{AgNO}_3$  aqueous-alcohol solution for 70 min. The Ag-coated por-Si was selected as the SERS substrate because it has been reported to provide ultrahigh sensitivity (up to a single molecule detection limit) combined with an extremely long shelf life (up to 3 years) due to por-Si surface features improving chemical stability of AgPs.

Morphology of the silvered samples was studied by using a scanning electron microscope (SEM) Hitachi-4800. Figure 1 clearly demonstrates that the obtained AgPs have various dimensions and shapes and are located at different distances from each other, forming a diversity of 3D silver structures.

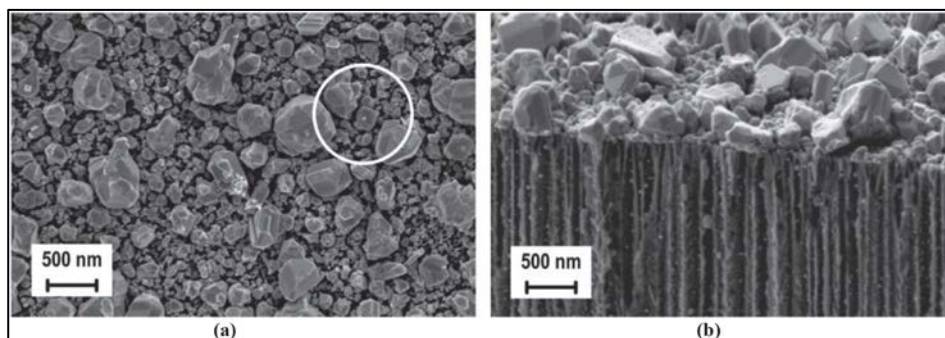


Fig.1. Characteristic SEM top view (a) and cross-section images (b) of the AgPs on the por-Si surface. The white circle illustrates the excitation laser beam spot (1  $\mu\text{m}$  in diameter) at the surface

Analysis of the SEM top view image (Figure 1a) with ImageJ software shows that the dimensions of 50% of the AgPs lie in the range from a few nanometers to 150 nm. However, the sample also contains the AgPs of 150–300 nm (~40%) and 300–600 nm (~10%) in cross-sectional dimension. The white circle in the image of Figure 1a indicates a possible location of the excitation laser beam spot of 1  $\mu\text{m}$  in diameter. It is obvious that in the experiment, a site with most likely numerous hotspots and many deposited reporter molecules is illuminated. As the reporter molecules, moieties of DTNB molecules ( $\text{C}_{14}\text{H}_8\text{N}_2\text{O}_8\text{S}_2$ ) represented in Figure 2 – TNB radicals – were employed in the experiments. The TNB/AgP conjugates were obtained by immersing an AgPs/por-Si sample into a  $10^{-5}\text{-M}$  solution of DTNB molecules in distilled water with ethanol for about 2h and then drying.

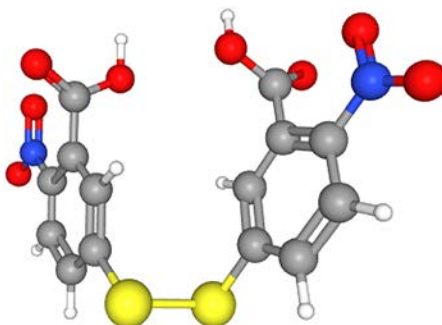


Fig.2. The 3D image of the molecular structure of a 5,5'-dithiobis(2-nitrobenzoic acid) molecule (DTNB) [<https://pubchem.ncbi.nlm.nih.gov/compound/6254#section=3D-Conformer>]

The S–S bond of the molecule breaks at the metallic surface, and the thiolates covalently bind to a surface of AgPs. Each particle can be coated with a large number of the reporter molecules estimated to exceed  $10^4$ . The TNB radicals are not absorbing excitation, anti-Stokes, or Stokes radiation. The strongest Raman lines in SERS spectra of the TNB correspond to the symmetric stretching vibration of the nitro group ( $\text{NO}_2$ ) and to the aromatic ring modes, and are shifted by, respectively, 1338, and 1070 and 1570  $\text{cm}^{-1}$ .

In order to characterize the homogeneity of TNB/AgP/por-Si SERS spectral profiles and spectral line strength distributions across the surface, 2D spectral maps (“matrices” of SERS spectra) were recorded. Typical dimensions of a mapping area were 10 x 10  $\mu\text{m}$  with the step of 1  $\mu\text{m}$ . Assuming that the areas of the hotspots are of the order of a few  $\text{nm}^2$ , the number of hotspots illuminated by the laser beam in a particular spatial point can vary from point to point between none and a large, but uncontrollable value (see Figure 1).

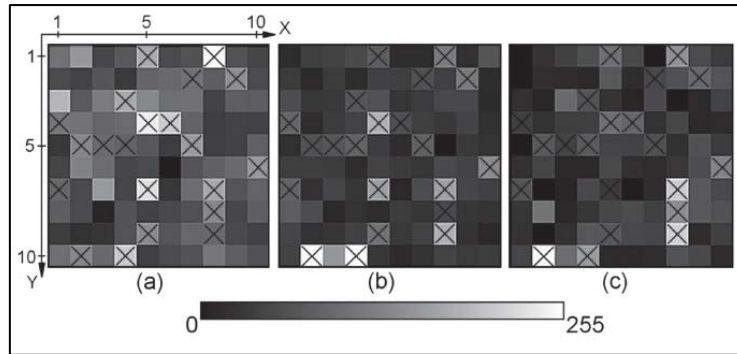


Fig.3. TNB line strength patterns for the wavenumbers (a) 1338, (b) -1338, and (c) -1070  $\text{cm}^{-1}$  at the laser intensity of  $I_L \approx 105 \mu\text{W}/\mu\text{m}^2$ ; the crosses mark some of the pixels where all the three lines are clearly observed

Figure 3 presents examples of 2D distributions of the strengths of the strongest TNB lines in the Stokes (with the wavenumber  $1338 \text{ cm}^{-1}$ ) and anti-Stokes (with the wavenumbers  $-1338$  and  $-1070 \text{ cm}^{-1}$ ) ranges of the SERS spectra plotted as a function of the beam focal spot spatial position. The corresponding map was recorded at the excitation intensity of  $I_L \approx 105 \mu\text{W}/\mu\text{m}^2$ , and each spectrum was accumulated during a short interval of 1 s.

The pattern in Fig. 3a shows that in the Stokes range, the strongest spectral line, at  $1338 \text{ cm}^{-1}$  is detected in about 45% of the spatial points. The other relatively strong Raman lines, at  $1070$  and  $1570 \text{ cm}^{-1}$ , which are, however, about three times weaker, are also detected in these points. At the same time, in the anti-Stokes range, whereas the lines with the wavenumber  $-1338 \text{ cm}^{-1}$  are observed in practically all the spatial points where the corresponding Stokes lines are detected. The weaker lines with the wavenumbers  $-1070 \text{ cm}^{-1}$ , and, especially,  $-1570 \text{ cm}^{-1}$ , are distinguished above the local background noise more rarely because of the small exposure time of 1 s used in the course of the mapping. Hence, even at the highest excitation intensity, the strongest Raman-resonant TNB peaks can be simultaneously registered in both Stokes and anti-Stokes ranges not in all the spatial points of the mapping area.

The appearance of the spectra is similar to that presented in Figure 4. The line strengths employed for building the patterns are calculated as the spectral amplitudes integrated within a gate of a definite spectral width after subtraction of a local spectral background. In each pattern, the line strengths are normalized by a maximal value.

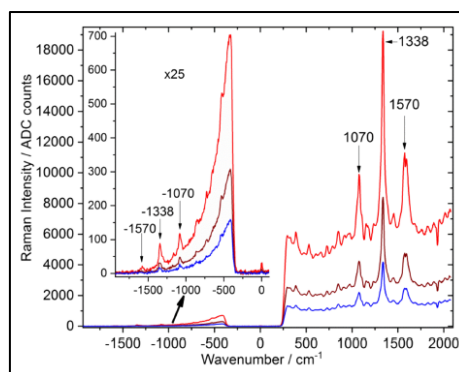


Fig.4. Anti-Stokes and Stokes SERS spectra of TNB/AgP/po-Si in a certain spatial point at excitation intensities 25, 51, and  $105 \mu\text{W}/\mu\text{m}^2$ ; the gap in the center of the spectra is defined by the notch-filter transmission.

To investigate the excitation-intensity dependence of the aS/S ratios more thoroughly, SERS spectra were recorded in definite spatial points, found in the course of the mapping to provide the largest line strengths, during longer exposure times of a few tens of seconds. The Raman shifts in the anti-

Stokes and Stokes ranges reached  $2000 \text{ cm}^{-1}$ . Figure 4 presents a few spectra, recorded at these different but low excitation intensities, at which the spectral profiles are still well reproducible. To verify the reproducibility while increasing the laser intensity, the spectra were repeatedly recorded at reduced intensities to ensure that the obtained spectrum resembles the one recorded earlier at the same intensity in both the spectral profile and TNB peak amplitudes. In the case of the AgP/por-Si SERS-active surface under study, the reproducibility range corresponded to excitation intensities  $I_L \leq 105 \text{ } \mu\text{W}/\mu\text{m}^2$ . In this range of intensities, all the variations of the SERS spectra were fully reversible, and neither spectral shifts of the strongest Raman lines nor any significant relative changes of their strengths were observed.

The strongest lines are assigned to the transitions of TNB molecules with the vibrational frequencies  $\nu_{R1} = 1570 \text{ cm}^{-1}$  (with the peaks at  $\lambda_{aS}/\lambda_S = 699/895 \text{ nm}$ ),  $\nu_{R2} = 1338 \text{ cm}^{-1}$  (with the peaks at  $\lambda_{aS}/\lambda_S = 710/877 \text{ nm}$ ), and  $\nu_{R3} = 1070 \text{ cm}^{-1}$  (with the peaks at  $\lambda_{aS}/\lambda_S = 724/857 \text{ nm}$ ). In Figure 4, the anti-Stokes parts of the spectra are also shown enlarged to demonstrate more distinctly the weak anti-Stokes Raman lines. Smaller ( $\sim 100$ – $600$  times) amplitudes of these lines are mainly determined by low populations of the upper vibrational levels at ambient temperature (295 K). To define the excitation-intensity dependences of the resonant line strengths, the latter were calculated as the peak heights above a local spectral background level approximated to the line centers. Such an approach was justified by the closeness of the linewidths.

### 1.2.2 Data analysis

The analysis of the experimental data describing the Stokes and anti-Stokes line strengths  $R_S$ , as dependences on the excitation intensity  $I_L$ , as those presented for a definite spatial point in Figure 5, shows that in the reproducibility range of excitation intensities ( $I_L < 105 \text{ } \mu\text{W}/\mu\text{m}^2$ ) the Stokes line strengths can, as expected, be described by linear dependences on laser intensity  $I_L$ :

$$R_{Si}(I_L) = B_i \cdot I_L, \quad (2)$$

whereas the anti-Stokes line strengths demonstrate the linear dependences on  $I_L$  only at low laser intensities, while at higher intensities can be described by quadratic polynomials of  $I_L$ :

$$R_{aSi}(I_L) = C_i \cdot I_L + D_i \cdot I_L^2, \quad (3)$$

where  $B_i$ ,  $C_i$  [count/s  $\times (\mu\text{m}^2/\mu\text{W})$ ], and  $D_i$  [count/s  $\times (\mu\text{m}^2/\mu\text{W})^2$ ] are the fitted coefficients of the dependences.

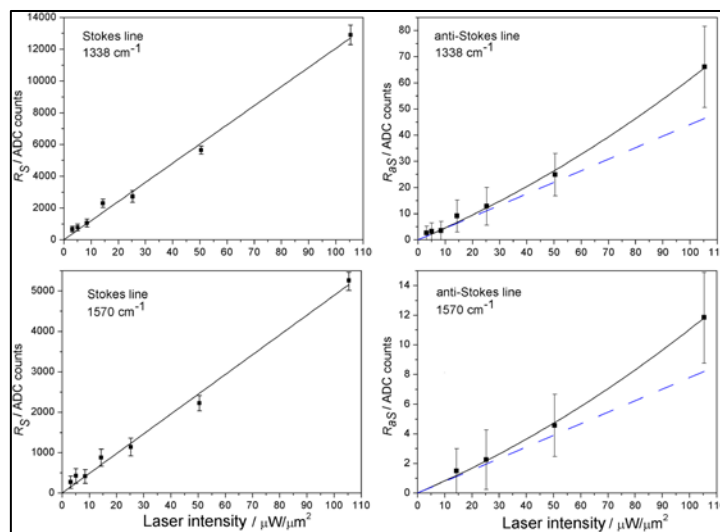


Fig. 5. The excitation laser intensity dependences of the Stokes and anti-Stokes line strengths in SERS spectra of TNB molecules at the AgPs/por-Si surface; squares – experimental data, solid lines – best fit linear (Equation 2, Stokes) and and quadratic (Equation 3, anti-Stokes) dependences. Blue dashed lines on the graphs represent the asymptotic linear contributions to the quadratic dependences of Equation 3.

Obviously, in the situation being considered, the aS/S ratios  $\rho_i(I_L) = R_{aS}/R_{St}$  will linearly depend on  $I_L$ :

$$\rho_i(I_L) = \rho_{0i} + \rho_{1i} \cdot I_L, \quad (4)$$

with the parameters  $\rho_{0i} = C/B_i$  and  $\rho_{1i} = D/B_i$  [ $\mu\text{m}^2/\mu\text{W}$ ]. Note, that employing the ratios is advantageous because it provides the possibility to exclude the numbers and spatial distributions of the hotspots and of the scattering molecules within the  $1\text{-}\mu\text{m}^2$  laser-illuminated area, which are difficult to be estimated or measured.

Figure 6 shows the spectra obtained in the experiments upon excitation of the sample separately by a cw and picosecond laser at the same power, as well as by their combination. Figure 6a shows the raw spectra, and Figure 6b – the spectra with subtracted luminescent background. It can be seen that the most intense Raman scattering lines in the SERS spectra of TNB correspond to the symmetric stretching vibration of the nitro group ( $\text{NO}_2$ ) and the modes of the aromatic ring, and are shifted by 1334, 1070, and 1570  $\text{cm}^{-1}$ , respectively.

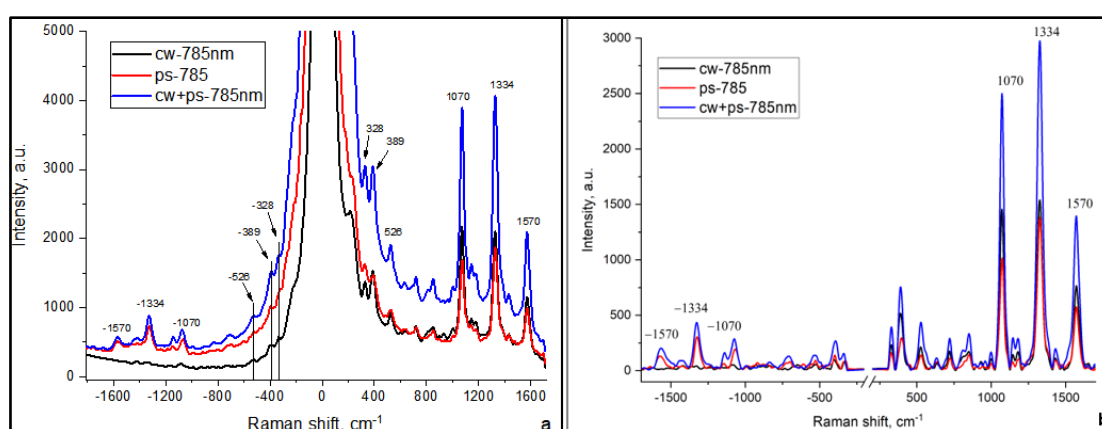


Fig.6. Anti-Stokes and Stokes SERS spectra of TNB molecules upon excitation by a cw and picosecond laser, as well as by their combination: a) unprocessed spectra, b) with subtraction of the luminescent background.

The discontinuity at the center of the spectra is determined by the transmission of the notch filter.

It is clearly seen from the results obtained that the intensity of the vibrational bands in the anti-Stokes part of the spectrum is significantly lower (at least by an order of magnitude) in the case of excitation by a cw laser compared to the picosecond one at the same pump powers in both cases. At the same time, in the Stokes part of the spectrum, the intensities of those bands are comparable in amplitude. In the case of combined pumping, the amplitudes of both the Stokes and the corresponding anti-Stokes components of the spectrum practically sum over the two pumps.

### 1.2.3 Conclusions

In this study it was experimentally shown that at 785 nm CW excitation laser intensities in the range of 3–105  $\mu\text{W}/\mu\text{m}^2$  Raman spectra of TNB reporter molecules at the randomly nanostructured SERS-active AgPs/por-Si surface are reproducible. This demonstrates the stability of the sample under investigation and provides possibility to measure the intensity dependence of the simultaneously recorded anti-Stokes and Stokes line strengths. The measurements show that in the reproducibility range the strengths of the Stokes and anti-Stokes TNB lines with the wavenumbers  $\pm 1070$ ,  $\pm 1388$ , and  $\pm 1570$   $\text{cm}^{-1}$  follow, respectively, a linear and a quadratic dependence on the excitation intensity.

The analysis of the anti-Stokes-to-Stokes line strength ratios as a function of the excitation intensity, found to be linear, allows to specify and estimate the contributions into these ratios of (i) the

plasmonic LFEF spectral profile, (ii) laser heating of TNB/AgP conjugates and (iii) local field enhanced optical Raman pumping of the TNB vibrational states. These three contributions are shown to account for the deviation of the ratios from the Boltzmann relation corrected by the scattering frequency factor.

Thus, in this study, it was experimentally shown that when the sample is excited by radiation at a wavelength of 785 nm, the ratio of the intensity of anti-Stokes to Stokes lines differs significantly depending on the pumping regime. An analysis of the intensity ratios of the anti-Stokes to Stokes lines depending on the pumping regime will make it possible to estimate the contributions to these ratios from (i) the plasmon spectral profile of the SERS substrate and (ii) the optical Raman pumping of TNB vibrational states.

## 2. Synthesis of lipodiscs / lipodiscs with embedded proteins and the study of their chemical structure and morphology by Raman spectroscopy.

One of the modern methods for isolating membrane proteins is the use of a styrene-maleic acid (SMA) copolymer. This amphipathic copolymer can integrate into biological membranes and easily destroy them. As a result, discoid membrane fragments with a size of 10-40 nm are formed, surrounded by a copolymer belt. Such particles are known as SMALPs (SMA lipid particles) or lipodiscs. The polymer has no affinity to any specific lipids, and, in SMALPs, the ratio of lipids remains the same as it was in the original membrane. The SMA-extracted membrane proteins are quite stable and can be purified and further analyzed by various biochemical methods. The benefit of SMA-extraction is the possibility of completely avoiding detergents in the protein purification process. It means better preservation of the native conformation and lipid microenvironment of the proteins. The preservation of the lipid microenvironment was demonstrated for a number of SMA-extracted proteins using thin-layer chromatography and mass-spectrometry. However, these methods are indirect and require the preliminary extraction of lipids from samples using mixtures of organic solvents with various additives. Presently, there is no universal extraction method that would be equally well suited for all lipid classes. Thus, it is necessary to select a specific methodology for the target class. Here, we used Raman spectroscopy and mass-spectrometry (MS) to analyze the presence of lipids in the lipodiscs stabilizing the recombinant human Kv7.1 protein. The recombinant human Kv7.1 protein was expressed in the HEK cell line. Elution fractions containing the Kv7.1 protein were combined and subjected to lipid extraction using a modified Folch method.

Unlike MS, Raman spectroscopy can be applied to intact lipodiscs. The system contains three chemically different components (SMA, Kv7.1, and lipids), and many of their Raman peaks overlap. So, it is quite complicated to attribute the observed peaks (Figure 7) to the vibrations of the chemical bonds of a specific component of the system. In particular, the Raman shift at  $\sim 1000\text{ cm}^{-1}$  can be attributed to either phenylalanine in Kv7.1, styrene in SMA, or C-H stretching in any of the three components.

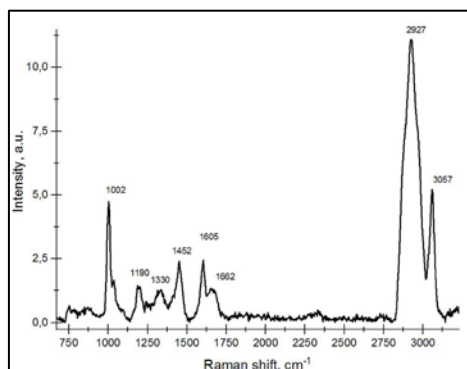


Fig.7. Raman spectrum of Kv7.1 containing SMALPs measured at 473 nm laser excitation.

However, the peak in the fingerprint region centered at  $1452\text{ cm}^{-1}$  ( $\text{CH}_2$  scissoring mode) and inherently strong peaks in the region of  $\sim 2800\text{--}3000\text{ cm}^{-1}$  indicate the presence of lipids and confirm the data obtained using MS. Thus, we have shown that when the recombinant Kv7.1 protein is isolated using SMA, it retains lipids around the protein molecules. MS confirmed that the lipids were present in the lipodiscs, and Raman spectroscopy detected several specific spectral peaks, which could be attributed to lipids. The Raman spectroscopy study of lipodiscs is still in progress.

### 3. Study of conformational changes in model lipid membranes embedded with various additives by Raman spectroscopy.

It's well-known, that addition of various molecules to the membrane can change its physical properties and alter its structure, which in turn may affect its functionality. Thus, it is crucial to know the origin of these changes and understand the intermolecular interactions responsible for embedding the various additives to the membrane.

In this study implemented in 2021, synthetic lipids were used, which are widely utilized to model the plasma membrane in order to study its properties. A model of a lipid bilayer containing DPPC phospholipid and its various combinations with cholesterol and melatonin molecules to best mimic natural cell membranes were created. Cholesterol and melatonin incorporate into the lipid bilayer at different positions. It has been proposed that melatonin resides in the head-group region of bilayer and thus, makes it more fluidic. On other hand, cholesterol should incorporate parallel into hydrocarbon chain region with its hydrophilic head close to the lipid's head-group. Such localization of cholesterol causes the membrane to become stiffer and thicker in the transverse direction because of the increasing order of hydrocarbon chains.

The Raman studies were performed with the samples prepared in the following way. DPPC in powder form was dissolved in a mixture of chloroform/methanol (2:1) at a concentration of 1 mg/ml. To completely remove the solvent from the obtained mixture, it was firstly kept in a stream of nitrogen gas and then placed in a vacuum overnight. In the next step, a thin film of DPPC on the bottom of the flask was mixed with 30 ml of distilled water utilizing a vortex shaker for 10–15 s to form a liposome suspension. At the last stage,  $10\text{ }\mu\text{l}$  of the analyte sample was dropped on the microscope quartz glass for the further Raman measurements.

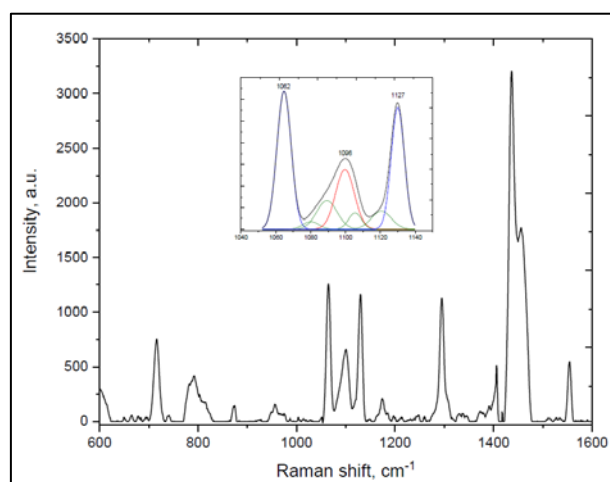


Fig.8. Raman spectrum of DPPC recorded with cw 532 nm excitation of 4mW. Top inset – deconvolution of the spectrum between  $1040$  and  $1150\text{ cm}^{-1}$  into 7 Gaussian lines consisting of two trans ( $1062\text{ cm}^{-1}$ ,  $1127\text{ cm}^{-1}$ , blue), one gauche ( $1096\text{ cm}^{-1}$ , red) and 4 Raman bands of choline group (green).

The samples were located at the motorized sample position adjustment stage (Prior Scientific, H117TE). The laser light was focused on the sample with a 40× objective (NA-0.6) in the  $\sim 1 \mu\text{m}$  spot. The laser power at the sample was controlled by a variable neutral filter with the 0–3 optical density. All the Raman spectra were collected in the backscattering geometry and dispersed by 1200-grooves-per-millimeter diffraction grating mounted in the MS520 monochromator-spectrograph. A Peltier-cooled charge-coupled device camera (ProScan HS-101H) was used for detection of the spectra collected at different localizations of the analytes. We probed signals in the  $600\text{--}1600 \text{ cm}^{-1}$  range of vibrational frequencies with the resolution of  $0.9 \text{ cm}^{-1}$  (Figure 8).

The Raman spectra in the interval between  $1030 \text{ cm}^{-1}$  and  $1150 \text{ cm}^{-1}$  was deconvoluted in 7 Gaussian lines. We evaluated spectral weights (i.e., integrated areas) of three of these lines for estimating the order/disorder dynamics in our systems. The Raman modes at  $1127 \text{ cm}^{-1}$  and  $1062 \text{ cm}^{-1}$  characterize asymmetric and symmetric vibrations of the carbon atoms and are known to originate from the trans structure. The Raman line at  $1096 \text{ cm}^{-1}$  is associated with the sensitivity of such vibrations with a single gauche defect and/or with the formation of various gauche isomers. Hence, the ratio of the spectral weights at  $1127 \text{ cm}^{-1}$  and  $1062 \text{ cm}^{-1}$  to that at  $1096 \text{ cm}^{-1}$  can be used to indicate the ratio of trans/gauche conformers of DPPC molecules. All measurements were performed at ambient temperature.

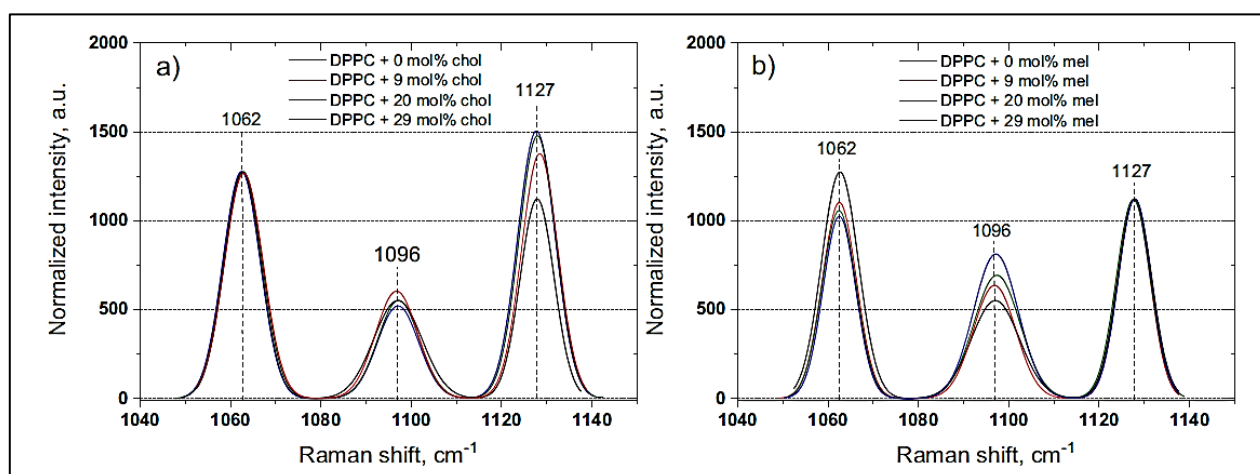


Fig. 9. Normalized Raman spectra of a) DPPC/cholesterol and b) DPPC/melatonin mixtures at various concentrations of the components (9, 20 and 29 mol%).

The normalized Raman spectra in the range of  $1030 \text{ cm}^{-1}$ – $1150 \text{ cm}^{-1}$  with the three dominant Raman bands for our systems are shown in Fig. 9a and 9b. We calculated the ratio of spectral weights at  $1127 \text{ cm}^{-1}$  to that at  $1096 \text{ cm}^{-1}$  ( $1127/1096$ ) for evaluating the ordering effect of cholesterol, while the ratio of spectral weights at  $1062 \text{ cm}^{-1}$  to that at  $1096 \text{ cm}^{-1}$  ( $1062/1096$ ) for evaluating the disordering effect of melatonin.

The input from the C–C stretching mode of the primary methyl groups of the hydrocarbon chain is best characterized by the ratio of the spectral weights  $1127/1096$ , while the increasing occurrence of gauche conformers is best evidenced in the ratio of spectral weights at  $1062/1096$ . The quantitative characteristics of the ratio of spectral weights as a function of the content of cholesterol and melatonin in DPPC bilayers are presented in Figure 10.

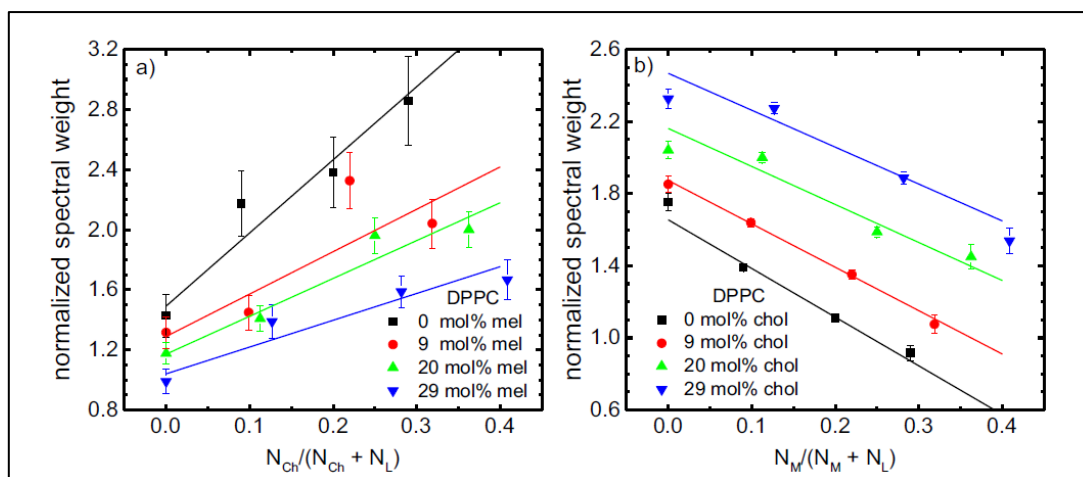


Fig.10. Dependencies of the ratios of trans/gauche conformers in DPPC bilayers as functions of the molar fractions of added (a) cholesterol and (b) melatonin. Black data present the effects of the compounds on the 2-component lipid bilayers. The colored data correspond to the bilayers loaded nominally with 9% (red), 20% (green), and 29% (blue) of melatonin or cholesterol. The curves are presented to guide the eyes.

Figure 10a presents a steep increase in the ratio of trans/gauche conformers upon the addition of cholesterol to the DPPC bilayers with no melatonin, clearly suggesting its rigidifying effect on the membrane. The effect of the cholesterol addition to the DPPC bilayers is modulated clearly by the additional presence of melatonin. This can be seen in the declining steepness of the trans/gauche ratio changes as a function of cholesterol concentration in the case of DPPC bilayers loaded with increasing amount of melatonin. Thus, the vibrational dynamics of lipid hydrocarbon chains is affected proportionally by both additives. The results presented in Fig. 10b for the DPPC bilayers with no cholesterol show straightforwardly the decreasing ratio of trans/gauche conformers upon increasing concentration of melatonin.

#### **Conclusions:**

- The vibrational dynamics of phospholipid hydrocarbon chains is affected proportionally (to some extent) by both additives: cholesterol and melatonin.
- The dynamic properties of the studied system indicate the predominant influence of cholesterol rather than melatonin.
- At high concentrations  $\sim 20\%$  and higher the fluidizing effect of melatonin is capable to inhibit the condensing effect of cholesterol.

#### **4. Synthesis of liposomes / liposomes with embedded proteins and the study of their chemical structure by Raman spectroscopy.**

##### **4.1. Formation of liposomes.**

Synthesis and formation of liposomes was carried out in accordance with the protocol modified by Avanti Polar Lipids (USA) for the synthesis of liposomes based on the instrument Vesicle Prep Pro - VPP, Nanion Technologies GmbH, Germany (<https://avantilipids.com/tech-support/liposome-preparation/giant-vesicle-preparation>).

In this work, DMPC phospholipid powder was used to synthesize liposomes, and chloroform (Sigma Aldrich) was used as a solvent. First, the phospholipid was dissolved in chloroform at a concentration of 3.4 mg/ml, and then 20  $\mu$ l of the dissolved phospholipid was deposited dropwise on the conductive side of the slide - an Indium Tin Oxide (ITO) glass slide. Next, the solvent was evaporated under vacuum for at least 60 minutes. After complete drying of the sample, a rubber sealing ring with a

diameter of 16 mm was installed on the ITO glass, which approximately corresponded to the outer contour of the deposited dried sample. After adding 250  $\mu\text{l}$  of bidistilled water to the ring, the slide was placed in the VPP electroformation chamber. The second ITO-glass was installed on top of the ring, and the so-called sandwich construct was thus ready for launching and formation of liposomes. The liposome formation protocol was run at a voltage of 3V and a frequency of 5Hz for 60 minutes at 37°C. The liposomes thus formed were carefully transferred to the eppendorf.

#### 4.2. Formation of the liposome/embedded peptide system.

To form a liposome system with an embedded peptide, the latter, after defrosting, was diluted drop by drop with a bidistilled water to a concentration of 1 mg/ml with a certain time interval. For electroformation of the liposome/peptide system, 250  $\mu\text{l}$  of the A $\beta$ (1-42) peptide dissolved in bidistilled water was added to the vacuum-dried phospholipid on an ITO glass slide with a rubber sealing ring installed. The second ITO glass, as in the previous case, was installed over the ring to form a sandwich structure. The liposome formation protocol was run at 3V and 5Hz for 60 minutes at 37°C. Upon completion of the protocol procedure, the liposomes with the embedded peptide were carefully transferred to the eppendorf.

#### 4.3. Results of the analysis of the liposome/peptide system by Raman spectroscopy.

Raman spectra of liposomes with embedded peptides were measured daily for four days to track the kinetics of the Raman frequencies. Of particular interest was the line Amide I (1620–1690)  $\text{cm}^{-1}$ , which is sensitive to conformational changes in the secondary structure of the peptide, as well as the spectral region of Raman frequencies in the range (1030–1150)  $\text{cm}^{-1}$ , where three bands characterizing the trans-gauche conformation in lipids are expressed. The results obtained are shown in Figure 11(a,b).

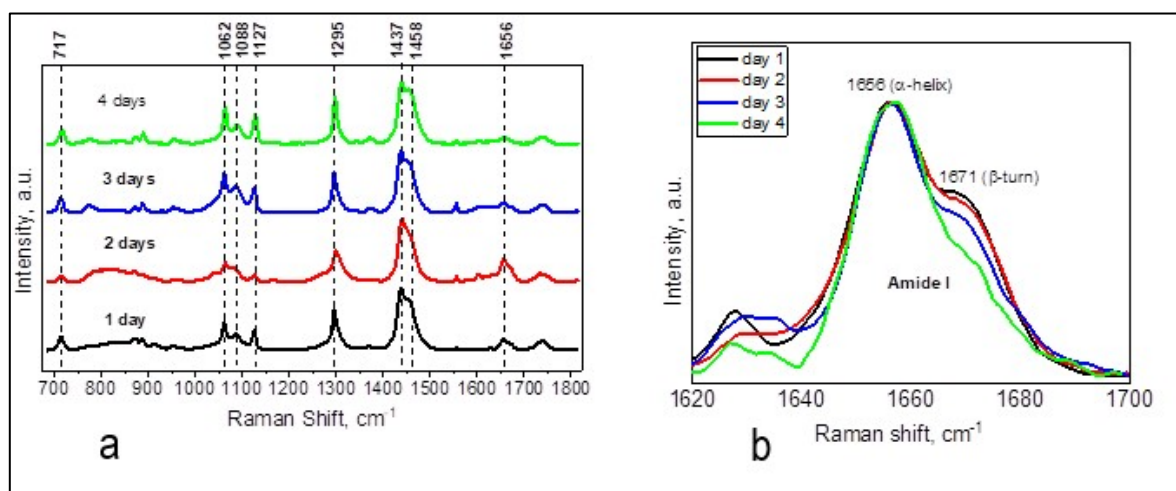


Fig.11. (a) Raman spectra of the liposome/peptide system by day, (b) normalized peptide spectra in the region of the Amide I line.

The normalized Raman frequencies in Fig. 11b clearly show that the intensity/spectral weight of the 1671  $\text{cm}^{-1}$  peak ( $\beta$ -turn, a type of irregular secondary structure in proteins) drops markedly by the 4<sup>th</sup> day of measurements, which indicates the conformation of the protein to a more stable structure with a characteristic Raman frequency at 1656  $\text{cm}^{-1}$  ( $\alpha$ -helix). It is known that the association of multiple beta-sheets/beta-turns can lead to protein aggregation and fibril formation, which is a precursor to Alzheimer's disease. Quantitative estimates of the ratio of the spectral weight of the  $\alpha$ -helix band and the beta-turn are given below in Table 1.

**Table number 1. Numerical ratios of the spectral weight of the  $\alpha$ -helix/ $\beta$ -turn by day.**

	Day 1	Day 2	Day 3	Day 4
$\alpha$ - helix/ $\beta$ - turn	2.1	2.4	2.8	3.3

The table shows that on the fourth day of measurements, the spectral weight of the conformational state of the peptide in the  $\alpha$ -helix increased by at least 1.5 times. This indicates that after balancing the liposome-embedded peptide system, the latter retains its natural conformational state.

## 5. Bio-chemically and light induced NETosis: Raman and fluorescent microscopy analysis.

### 5.1. Bio-chemically induced NETosis.

The research activities in 2021 were devoted to the application of Raman spectroscopy and immunofluorescent microscopy analysis of neutrophils transformed during NETosis and the quantitative determination of the level of their transformation based on the analysis of the neutrophil Raman spectra.

Kinetic analysis with highly sensitive vibrational spectroscopy applied for this study, revealed in the low-frequency range of the neutrophil cells Raman spectrum the evolution (growth) of the citrulline peak within 30-40 minutes after the beginning of the inflammatory process, which can be classified as an early diagnosis of NETosis (Figure 12).

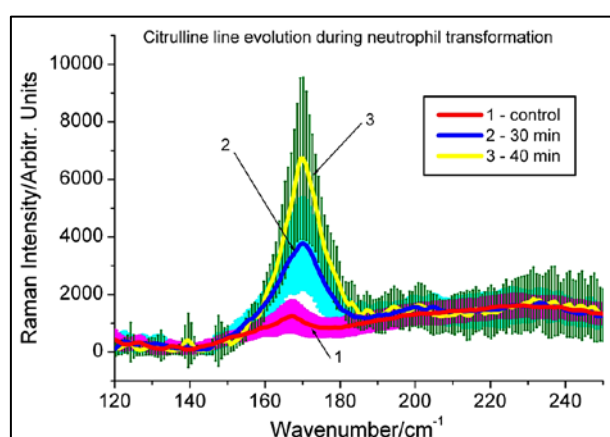


Fig.12. Low-frequency region of Raman spectra of neutrophils: citrulline line evolution (growth) indicating the pre-activation of NETosis.

Because the peak with the Raman shift of  $\sim 170$   $\text{cm}^{-1}$  is practically absent in inactivated neutrophils and increases significantly after activation, one can assume that it is associated with the accumulation of citrulline in the cell, the spectrum of which also has a characteristic peak around  $170\text{cm}^{-1}$ . Normally, citrulline is practically absent in human cells because it is not one of the 20 basic amino acids from which the proteins of our body are built. However, it is known that during NETosis, citrulline could be produced, first of all, by transformation of histones, the most important structural chromosomal proteins inside neutrophil nuclei.

### 5.2. UVA and visible light induced NETosis.

In continuation of the initiated study on the activation of neutrophils by two approaches: biological (bacterial) and chemical (PMA) stimuli, in 2021-2022 we came over to examine the ability of neutrophils to realize NETs under the UVA and visible light irradiation. Human neutrophils were isolated from the

whole blood obtained from healthy voluntary donor. In the novel set of the experiments we applied UVA and visible light irradiation in a dose-dependent manner. Data analysis was done implementing fluorescence microscopy and Raman spectroscopy.

### **5.2.1. Isolation and irradiation of neutrophils**

Peripheral blood was taken from healthy donors by their verbal consent and placed in EDTA blood collection tubes. Neutrophils were isolated by centrifugation in a double density gradient using ficoll solutions with a density of 1.077 g/cm<sup>3</sup> and 1.119 g/cm<sup>3</sup>. Next, 3 ml of ficoll with a density of 1.077 g/cm<sup>3</sup> was carefully layered on top of 3 ml of ficoll of 1.119 g/cm<sup>3</sup> in a 10 ml tube. 4 ml of undiluted blood was layered onto the resulting stepwise density gradient. The tube was centrifuged at 400 g for 40 min at room temperature. The resulting layer of neutrophils was carefully taken with a pipette into a 10 ml tube, then the liquid volume was adjusted to 10 ml with PBS. The suspension of neutrophils was centrifuged at 250 g for 8 min. The supernatant was removed and 9 ml of bidistilled water (4 C°) was added to the neutrophil sediment to lyse the remaining erythrocytes. The suspension was again centrifuged at 250 g for 8 min. Neutrophils were resuspended in RPMI 1640 nutrient medium to a concentration of 1x10<sup>5</sup> cells/ml.

The isolated neutrophils were irradiated with a WheelLED Wavelength-Switchable LED Sources (Mightex) illuminator at the following wavelengths: 365 nm (UVA, WLSLED-0365-04), 405 nm (blue light, WLS-LED-0405-03), 530 nm (green light, WLS-LED-0530-03), 625 nm (orange light, WLS-LED-0625-03), and 656 nm (red light, WLS-LED-0656-03). The cells were irradiated at RT in a selected dose-dependent manner: 4, 16, and 32 J/cm<sup>2</sup>. The irradiation power of the LEDs was measured using a PM100A powermeter (Thorlabs, USA).

### **5.2.2. Raman spectroscopy**

In this study, Raman spectroscopy was used to measure the spectra of radicals, in particular, H<sub>2</sub>O<sub>2</sub> and HClO. Both for point spectral measurements of spontaneous Raman scattering and for mapping with excitation by a helium-neon laser with a wavelength of 633 nm, a confocal microspectroscopy setup with a high spectral resolution and a high scanning speed of the laser spot was used. It includes a scanning laser spectrometer "Confotec CARS" (LLC "SOL Instruments", Belarus), coupled with an inverted microscope NIKON TE2000-E.

### **5.2.3. Visualization of NETs with fluorescence microscopy**

To examine netosis levels, cells were washed twice with PBS and then neutrophilic DNA was stained with DAPI dye for 10 min. After staining, cells were washed with 1% PBS. Images were photographed in a 96-well plate using a Nikon Eclipse Ts2R-FL fluorescent LED microscope using NIS-Elements BR software, an Epi-FL C-LED385 filter, and a 20x CFI Super Plan Fluor ELWD ADM objective with a numerical aperture of 0.45 and working distance (8.2–6.9) mm. Twenty frames were captured in each well. The total number (by 20 frames) of netotic and intact cells was counted using ImageJ software.

### **5.2.4. Main results on light induced NETosis: Raman spectroscopy and fluorescence microscopy**

The primary ROS in activated neutrophils are superoxide O<sub>2</sub><sup>-</sup> anions, which, being weak oxidizing agents, quickly dismutate to hydrogen peroxide H<sub>2</sub>O<sub>2</sub>. These, in turn, can be further processed to form more active metabolites, such as hydroxyl radical (OH·) and hypochlorous acid (HOCl). To confirm

the role of ROS in the formation of NETs in our experiments, we used Raman spectroscopy to detect a sharp Raman peak characteristic of hydrogen peroxide in the region of 875-880  $\text{cm}^{-1}$  (O–O stretch) and hypochlorous acid at a Raman frequency of  $\sim 732 \text{ cm}^{-1}$ . The measurements were carried out in the mapping mode when neutrophils were excited by a He-Ne laser at a wavelength of 632.8 nm during the first 10-15 minutes after their activation by LEDs at different wavelength and at a dose of  $32 \text{ J/cm}^2$ . An example is shown in the Figure 13.

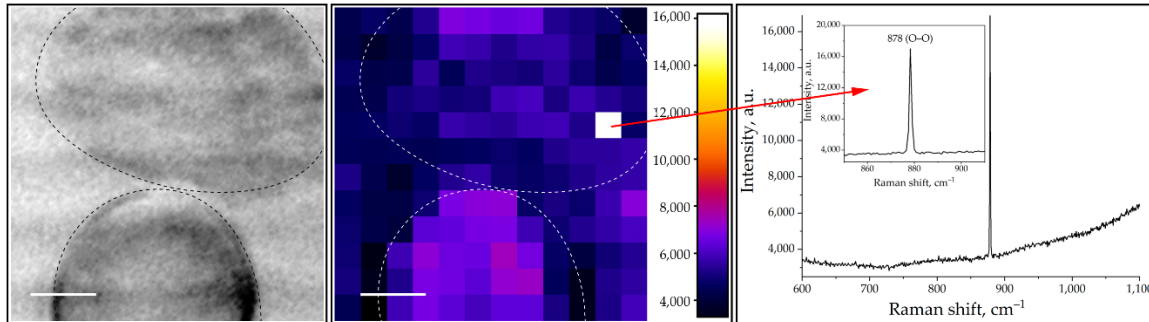


Fig. 13. Micrograph (left), Raman map (middle), and spectrum (right) of neutrophils exposed to radiation with a wavelength of 625 nm and a dose of  $32 \text{ J/cm}^2$ . The characteristic sharp lines of  $\text{H}_2\text{O}_2$  can be seen on the right. The spectral gate was aligned within the interval of  $872\text{--}882 \text{ cm}^{-1}$ . Scan area  $24 \times 24 \mu\text{m}$ , bars:  $5 \mu\text{m}$ .

Figure 13 (middle) shows one of the Raman maps we obtained for irradiated cells at a wavelength of 625 nm and at a dose of  $32 \text{ J/cm}^2$ . Spectral gates were set in the range of  $872\text{--}882 \text{ cm}^{-1}$  in order to search for and record the characteristic narrow peak of hydrogen peroxide. The map shows positive pixels with mostly low or moderate intensity at the Raman frequency of  $878 \text{ cm}^{-1}$  ( $\text{H}_2\text{O}_2$ , O–O stretch) and one bright pixel with a corresponding sharp peak shown in the spectrum on the right.

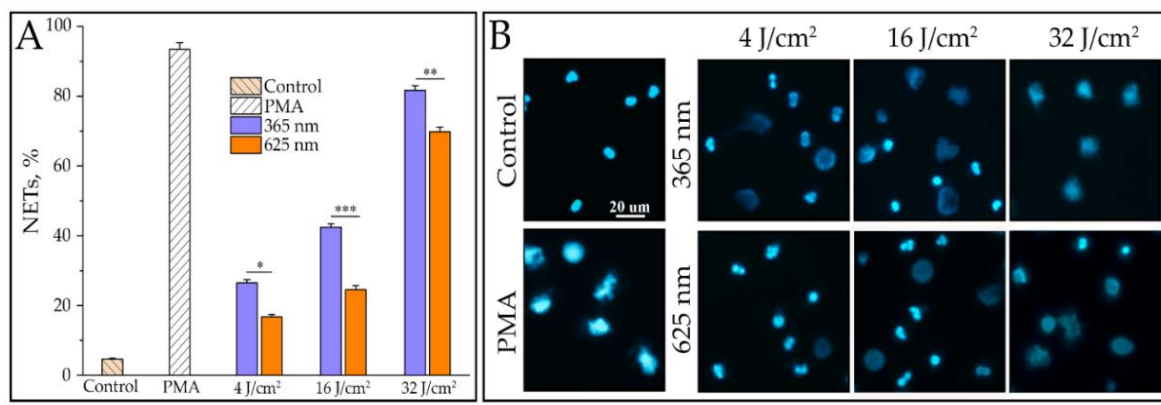


Fig.14. Release of NETs depending on dose at wavelengths of 365 nm and 625 nm [A], and corresponding fluorescence images [B]. Bar:  $20 \mu\text{m}$ .

Figure 14A shows that the NETs yield is dose-dependent when neutrophils are irradiated at UVA (365 nm) and visible light (625 nm). The results of the positive (PMA) and negative (non-irradiated cells) controls are presented in the figure as well. The corresponding fluorescence microscopy images are shown in Figs. 14b.

In order to elucidate whether NADPH oxidase is involved in NET formation induced under light radiation, we used a specific inhibitor of NADPH oxidase – apocynin. We also wanted to elucidate whether PAD4 is engaged in light-induced NET formation. For this, we used a specific inhibitor of PAD4, GSK484. The results are presented in Figure 15.

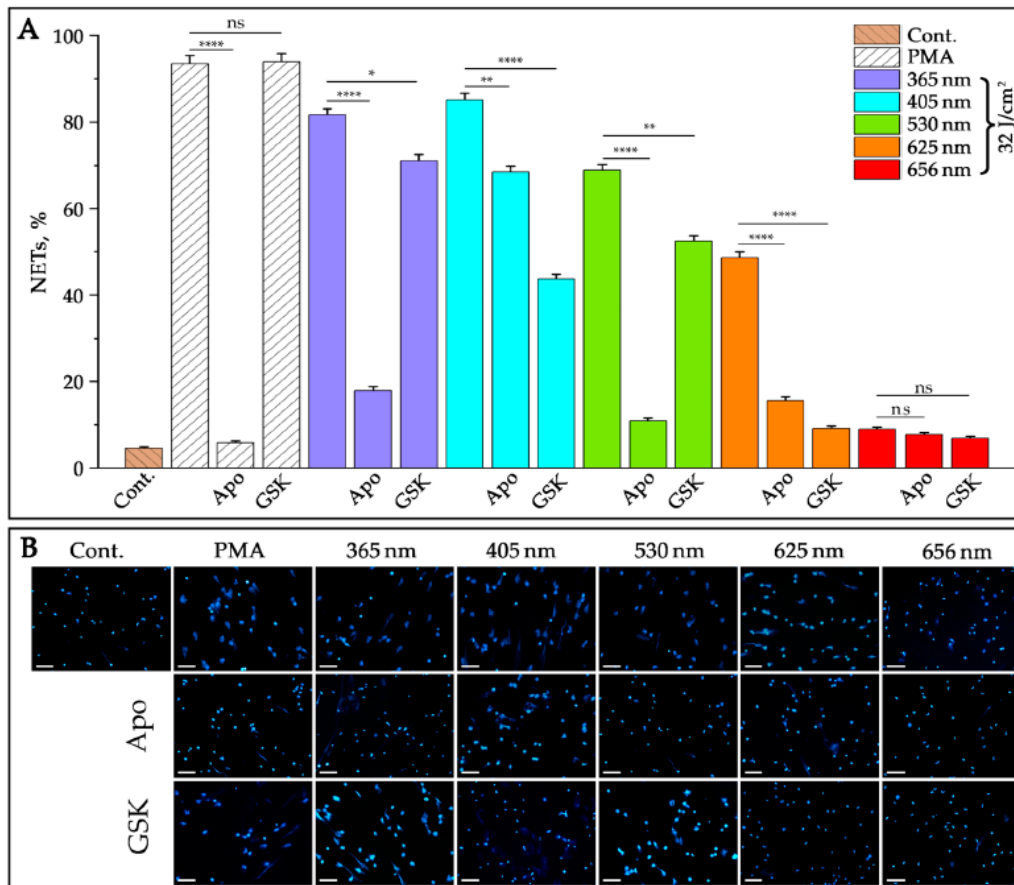


Fig.15. Effects of selective inhibitors of NADPH oxidase (apocynin) and PAD4 (GSK484) on NET formation in neutrophils irradiated with five LED-lengths of 365, 405, 530, 625, and 656 nm and the same energy dose of 32 J/cm<sup>2</sup>. PMA (50 nM) was used as a positive control. After incubation for 3 h, the cells were stained with DAPI and analyzed using fluorescence microscopy.

As can be seen in Figure 15, apocynin inhibits NET formation induced by UV-A and three wavelengths of visible light (blue, green, and orange), indicating the involvement of NADPH oxidase in light-induced NETosis. As for the inhibitor of PAD4, GSK484 – it caused moderate suppression of NETosis, indicating the involvement of PAD4 in light-induced NET formation.

### 5.2.5. Conclusion

In the present study, we focused on the role of radiation with different wavelengths to induce NET formation on the model of human neutrophils. We discovered for the first time that not only UVA, but also visible light (blue, green, and orange) induced the release of NETs. Using specific inhibitors of NADPH oxidase and PAD4, we demonstrated that these mediators of classical NETosis are involved in NET release induced by light radiation. Therefore, ROS formation and histone citrullination contribute to chromatin decondensation in this setting. Fluorescence microscopy results showed dose-dependent formation of netotic cells. Raman spectroscopy was used to register oxidative stress and ROS generation for the first time.

The most likely photoacceptor and transducer of photo signals, in our opinion, is the membrane-bound heterodimeric flavohemoprotein cytochrome *b<sub>558</sub>*, a structural component of NADPH oxidase, which contains redox centers.

## 6. Detection of low-frequency Raman spectra using volumetric Bragg filters simultaneously in Stokes and anti-Stokes regions.

At present, most of the research on Raman spectroscopy is aimed at studying intramolecular vibrations whose Raman shifts exceed  $100\text{ cm}^{-1}$ . At the same time, low-frequency Raman spectroscopy is very promising for studying a wide range of materials and makes it possible to obtain important information about them. For example, in polymers, these are longitudinal acoustic modes; in various crystals, vibrations in crystal lattices; in carbon nanotubes, radial fully-symmetric modes; in semiconductor materials, acoustic phonons; in gases, rotational modes; in DNA, vibrations of the skeleton; in pharmaceutical tablets – low-frequency characteristic oscillations, etc.

Registration of Raman spectra in the low-frequency region is associated with difficulties in detecting a weak Raman signal against the background of a strong Rayleigh scattering signal. Existing "notch" filters have a band of about  $300\text{ cm}^{-1}$  (Fig.16, curve 1), which limits the possibility of measuring spectra in the low-frequency region. Long-wavelength transmissive "edge" filters make it possible to get closer to the laser line (Fig.16, curve 2), but a certain fraction of the more intense Rayleigh radiation enters the spectral detector.

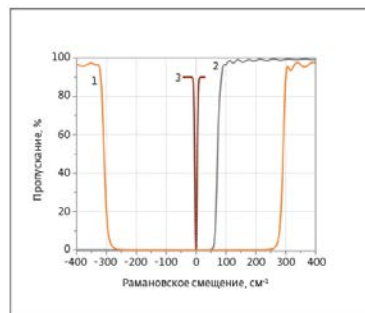


Fig.16. Transmission band of various Raman filters: Semrock "notch" NF01-633E-25 (curve 1), Semrock "edge" LP02-633RE (curve 2), OptiGrate BragGrate BNF-633 (curve 3).

Special filters based on BragGrate volumetric Bragg gratings, which are characterized by high selectivity, were used to separate the low-frequency Raman signal against a strong background of Rayleigh scattering on the CARS microspectrometer of the FLNP (Fig. 16, curve 3). The advantages of such filters are their ultranarrow pass-band ( $\sim 5\text{ cm}^{-1}$ ), a high degree of attenuation of the exciting laser radiation (optical density  $>4$ ) and transparency for Raman signals (up to 85%), which allows them to be used to study ultralow frequency spectra ( $<50\text{ cm}^{-1}$ ) in systems with single monochromators. Another advantage of such filters is the possibility to simultaneously record the Stokes and anti-Stokes components in the Raman spectrum. Figure 17 shows examples of such spectra.

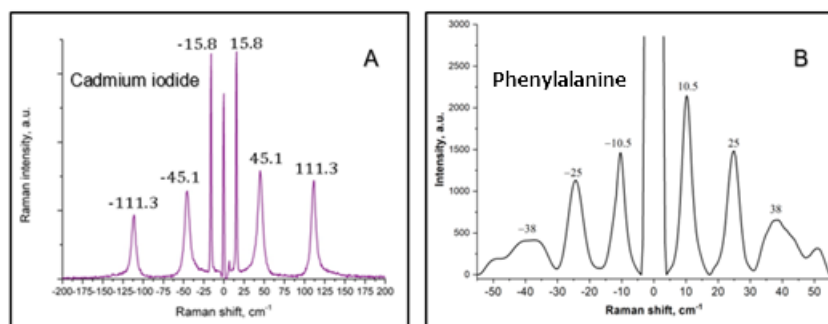


Fig.17. Low frequency Raman spectrum of (A) cadmium iodide, a narrow peak at  $15.8\text{ cm}^{-1}$  is the  $E_2$  mode of the 4H polytype; (B) phenylalanine: lattice modes

**Conclusion:** As a result of our studies, we have demonstrated the efficiency of using Bragg volumetric filters in the CARS microspectrometer for recording ultralow-frequency spectra ( $<30\text{ cm}^{-1}$ ) of various materials when samples are excited by a laser at a wavelength of 633 nm.

## Publications 2021 – 2023

1. Arzumanyan G.M., Mamatkulov K.Z., Vorobyeva M.Y., et al., "Plasmon resonance, thermal, and optical contributions to anti-Stokes-to-Stokes line strength ratios in continuous wave-excited surface-enhanced Raman scattering spectra of molecules at random Ag surface", *J Raman Spectroscopy*, **2021**, 52, 1515–1528, [doi.org/10.1002/jrs.6190](https://doi.org/10.1002/jrs.6190), (Microspectrometer "CARS").
2. Baibarac M., Arzumanyan G.M., Daescu M., et al., "Anisotropic Photoluminescence of Poly(3-hexyl thiophene) and Their Composites with Single-Walled Carbon Nanotubes Highly Separated in Metallic and Semiconducting Tubes", *Molecules*, **2021**, 26, 294, [doi.org/10.3390/molecules26020294](https://doi.org/10.3390/molecules26020294), (Microspectrometer "CARS", partially).
3. Kondela Tomas, Dushanov Ermuhammad, Vorobyeva Maria, et al., "Investigating the competitive effects of cholesterol and melatonin in model lipid membranes", *BBA*, **2021**, Biomembranes 1863, 9, [doi.org/10.1016/j.bbamem.2021.183651](https://doi.org/10.1016/j.bbamem.2021.183651), (Microspectrometer "CARS", partially).
4. Karlova M., Bagrov D., Vorobyeva M., et al., "Raman spectroscopy reveals lipids in protein-containing SMA-stabilized lipodiscs", (Microspectrometer "CARS"), *Microsc. Microanal.*, **2021**, 27 (Suppl 1), [doi:10.1017/S1431927621006267](https://doi.org/10.1017/S1431927621006267).
5. Siarhei Zavatski, Hanna Bandarenka, Łukasz Hetmanczyk, Joanna Hetmanczyk, Maria Vorobyeva, Yersultan Arynbeke, Kahramon Mamatkulov, Grigory Arzumanyan, "Model phospholipid interaction with cholesterol and melatonin: Raman spectroscopy and density functional theory study", *J Raman Spectroscopy*, **2022**, 53 (9) 6 1540-1550, [DOI: 10.1002/jrs.6409](https://doi.org/10.1002/jrs.6409), (Microspectrometer "CARS").
6. Anka Jevremovic, Ana Stanojkovic, Dragana Arsenijevic, Aleksandar Arsenijevi, Grigory Arzumanyan, Kahramon Mamatkulov, et al., "Mitigating toxicity of acetamidrid removal techniques – Fe modified zeolites in focus" *Journal of Hazardous Materials*, **2022**, 436, [doi.org/10.1016/j.jhazmat.2022.129226](https://doi.org/10.1016/j.jhazmat.2022.129226), (Microspectrometer "CARS", partially).
7. Grigory Arzumanyan, Kahramon Mamatkulov, Yersultan Arynbeke, Darya Zakrytnaya, Anka Jevremović, Nina Vorobjeva, "Radiation from UV-A to Red Light Induces ROS-Dependent Release of Neutrophil Extracellular Traps", «International Journal of Molecular Sciences», **2023**, Volume 24, Issue 6, 5770, [doi.org/10.3390/ijms24065770](https://doi.org/10.3390/ijms24065770), (Microspectrometer "CARS").
8. Hanna Bandarenka, Siarhei Zavatski, Yersultan Arynbeke, Kahramon Mamatkulov, Grigory Arzumanyan, «Conformational analysis of molecular systems based on liposomes and lipodiscs modified with A $\beta$ -peptide (1-42) by Raman spectroscopy and computer modeling», **2023**, submitted to the Journal "Biomembranes". (Microspectrometer "CARS", partially).
9. Sergei Kurakin, Dina Badreeva, Sergey Efimov, Timur Mukhametzyanov, Ermuhammad Dushanov, Tatiana Murugova, Oleksandr Ivankov, Darya Zakrytnaya, Artyom Shutikov, Kahramon Mamatkulov, Norbert Kočerka, "Arrangement of lipid vesicles and bicelle-like structures formed in the presence of A $\beta$ (25-35) peptide", **2023**, in preparation.

## Conferences 2021 – 2023

1. Arzumanyan G.M., "Search of Raman markers of NETosis, 15-16 Sept., **2021**, Cairo, Egypt, **keynote plenary report** (online).
2. Vorobyeva M.Yu., "The dynamical properties of DPPC lipid bilayer: Raman spectroscopy characterization", 33<sup>rd</sup> Nano congress for Future Advancements, 28-29 April **2021**, London, UK, oral section report (online)
3. Arynbeke Y., "Combined study of lipid bilayers by Raman spectroscopy, neutron scattering and MD simulation", YOUNG MULTIS - Multiscale Phenomena in Condensed Matter - conference for young researchers, 5-7 July **2021**, Krakow, Poland, oral section report (online).
4. Mamatkulov K., "Raman study of conformational changes in phospholipids", 20-24 Sept., **2021**, Almaty, Kazakhstan, Oral report (online)
5. Arynbeke Y., Arzumanyan G.M., "Competitive effect of cholesterol and melatonin in incorporated in lipid membrane: Raman characterization", 11-15 Oct., **2021**, Almaty, Kazakhstan, oral section report
6. Arzumanyan G.M., "CARS microspectroscopy in biomedical applications", 4th Global Webinar on Applied Science, Engineering and Technology (WEBAS-2022)", 22-23 October, **2022**, Live Stream, online.

7. Mamatkulov K.Z., "Synthesis and characterization of green nanofiber-based composite materials", 5th International Caparica Symposium on Nanoparticles/Nanomaterials and Applications, 24-27 January **2022**, Caparica, Portugal, online.
8. Arynbeq Y., "Investigation of the Structure and Dynamics of Complex Membrane Systems by Neutron and Raman Scattering Techniques", International Workshop on Nuclear and Particles Physics, 24-30 April, **2022**, Almaty, Kazakhstan, Oral report.
9. Arynbeq Y., Investigation for spectral biomarkers: chemical, UV and light induced NETosis", JINR Association of Young Scientists and Specialists (AYSS), "Alushta-XI", 5-12 June, **2022**, Alushta. Oral report.
10. Zakrytnaya D.S. Photoinduced neutrophil extracellular traps, VII Congress of Biophysicists of Russia, 17-23 April, **2023**, Krasnodar. Poster.
11. Shutikov A.A. Investigation of conformational changes in peptide A $\beta$ (1-42) by Raman spectroscopy, VII Congress of Biophysicists of Russia, 17-23 April, **2023**, Krasnodar. Oral report.
12. Mamatkulov K.Z., "Photo-Induced Neutrophil Extracellular Traps: The Role of Cytochromes", International Conference on Radiation applications, May 29 - June 2, **2023**, Anavyssos, Greece

## **Educational program 2021 – 2023 at the Sector of Raman spectroscopy**

### **Student summer practice programme:**

1. Student Daria Kravtsunova, 2021
2. Student Anna Geronina, 2022
3. Student Alyona Kisina, 2022, 2023

**Training:** Kurbonov Sarvar Sanzhar – 6-month training, May-November 2022, Uzbekistan.

### **Research work**

1. Anna Geronina, topic: "Photosynthesis in plants and bacteria" 03.2022 - 05.2022.
2. Alyona Kisina, topic: "Ap-conversion photoluminescence in 2D materials and Van der Waals heterostructures" 2023.

### **Bachelor's work**

1. Anna Geronina, "Investigation of 2D materials and van der Waals heterostructures by Raman spectroscopy", 2023.

## **International cooperation on the topic 1133:**

Armenia, Republic of Belarus, Bulgaria, Egypt, India, Cuba, Poland, Russia, Romania, Serbia, Slovak Republic, Uzbekistan, Ukraine within the framework of cooperation programs or grants.

## **Theme support by the Plenipotentiaries of the JINR Member States in the form of grants and cooperation programs:**

In 2021-2023, theme # 1133 was supported by the Plenipotentiaries of the following countries in different years: Bulgaria, Poland, Romania, Serbia, Slovak Republic.

### **Theme leaders:**

\_\_\_\_\_ G.M. Arzumanyan

\_\_\_\_\_ N. Kučerka